CrossMark

X-ray spectroscopic and stroboscopic analysis of pulsed-laser ablation of Zn and its oxidation

Stefan Reich[1] · Jörg Göttlicher[1] · Alexander Letzel[2] · Bilal Gökce[2] · Stephan Barcikowski[2] · Tomy dos Santos Rolo[1] · Tilo Baumbach[1,3] · Anton Plech[1] (ORCID)

Abstract

Pulsed laser ablation in liquids (PLAL) as an attractive process for ligand-free nanoparticle synthesis represents a multiscale problem to understand the mechanisms and achieve control. Atomic and nanoscale processes interacting with macroscale dynamics in the liquid demand for sensitive tools for in-situ and structural analysis. By adding X-ray methods, we enlarge the available information on millimeter-scale bubble formation down to atomic-scale nanoparticle reactions. X-ray spectroscopy (XAS) can resolve the chemical speciation of the ablated material during the ablation from a zinc wire target showing a first oxidation step from zinc to zinc oxide within some 10 min followed by a slower reaction to hydrozincite. X-ray imaging investigations also give additional information on the bubble dynamics as we demonstrate by comparing the microsecond radiography and optical stroboscopy. We show different features of the detachment of the ablation bubble from a free wire. The location of the first collapse occurs in front of the target. While a first rebound bubble possesses an homogeneous interior, the subsequent rebound consists merely of a cloud of microbubbles.

1 Introduction

Due to its large direct band gap, zinc oxide (ZnO) nanoparticles (NP) are used in many fields in opto-electronics, photonics and biomedical applications [1–6]. Synthesizing ZnO NPs by PLAL [7–10] has the great advantage of obtaining a residue-free dispersion as compared to chemical synthesis [11]. The ablated particles from a pure zinc (Zn) target undergo an oxidation to ZnO where the water is supposed to deliver the oxygen [5, 12]. Few studies investigated this oxidation during and directly after ablation [5, 6]. Access to kinetics was given by optical extinction spectroscopy. With X-ray absorption spectroscopy (XAS), a better understanding of processes can be obtained due to the fact that XAS is directly sensitive to the targeted element, its valency state and local environment, therefore, allows to address elemental speciation [13], in particular oxidation state.

Increasing the ablation yield is a major point for industrial applications [14]. Therefore, the manipulation of the bubble dynamics for a better release of the NPs into the water is of big interest [15–17]. Imaging the fast bubble dynamics requires a high time resolution such as obtained by stroboscopy [18, 19] or light emission [20–22]. A more quantitative analysis also requires a high penetration and nanoscale resolution, which again X-ray investigation can deliver [16, 23–25].

Within this communication, a first exploration of XAS together with imaging methods targets the production of Zn-based particles by PLAL to identify Zn and display the process of oxidation of it. We show that the dynamics of detaching ablation bubble on a wire target include an efficient ejection and thus minimized redeposition.

✉ Anton Plech
anton.plech@kit.edu

1 Institute for Photon Science and Synchrotron Radiation, KIT Karlsruhe, Postfach 3640, 76201 Karlsruhe, Germany

2 Technical Chemistry I and Center of Nanointegration Duisburg-Essen (CENIDE), University of Duisburg-Essen, Universitätsstrasse 7, 45141 Essen, Germany

3 Laboratory for Application of Synchrotron Radiation, KIT Karlsruhe, Engesser Straße 15, 76131 Karlsruhe, Germany

2 Experimental details

PLAL setup The ablation is performed in a small-volume flow chamber (0.5 ml) with optimized channels for water flow, laser coupling and target transport for the stroboscopy and X-ray radiography. Water is continuously pumped through the volume to replace the suspension completely before each laser shot. A plano-convex lens (Thorlabs) focuses the laser onto the target (effective focal length in water 38 mm) and acts also as chamber enclosure (sealed by an O-ring) [24]. The target consists of a Zn wire (Advent, 99.9 %) with 1 mm in diameter, continuously fed through the chamber for a clean surface at each shot. For the experiment on the oxidation kinetics, the ablation was done in a fixed batch chamber with 1.5 ml of ultrapure water (Millipore) with only the wire being transported. After a 1 min ablation at 15 Hz, a part of the suspension was transferred to a probe chamber within the X-ray spectroscopy experiment (cylindrical polymer beaker with 3 mm thickness) and a cuvette (5 mm path length, PMMA) for the UV–Vis spectroscopy, respectively.

The laser source consists of a Q-switched Nd:YAG laser operated at the 1064 nm fundamental wavelength (Continuum Minilite I). A pulse energy of 11 mJ for imaging and 25 mJ for spectroscopy were used, respectively.

Microsecond imaging Imaging with visible light was performed in stroboscopic mode with a Xenon flash lamp (Rheintacho, 5 µs flash duration) and a visible-light CMOS camera (Basler, 1280×960 pixels of 5 µm size). The locus of ablation was imaged by a 50 mm TV lens (Ernitec) in an 1:1.2 magnification. A diffuser between flash and chamber avoided inhomogeneous illumination. The delay between laser, flash and camera was controlled by a delay generator (Research Instruments DG535).

X-ray radiography was performed at the synchrotron at KIT (Karlsruhe, Germany) on the tomography instrument TOPO-TOMO [26]. The sample was continuously irradiated by a broad, white X-ray beam, while an active-pixel detector (PCO.dimax) was used to record the signal (optical photons from a scintillator) at a frame rate of 10 kHz and exposure time of 30 µs. With a fourfold interleaving of movies of shifted temporal delay an effective frame rate of 40 kHz was achieved. After dark-current subtraction and flat corrections the images were averaged over 50 successive laser shots.

Figure 1 shows selected frames of the movies. Note that due to flat-field correction, no signal is left at the position
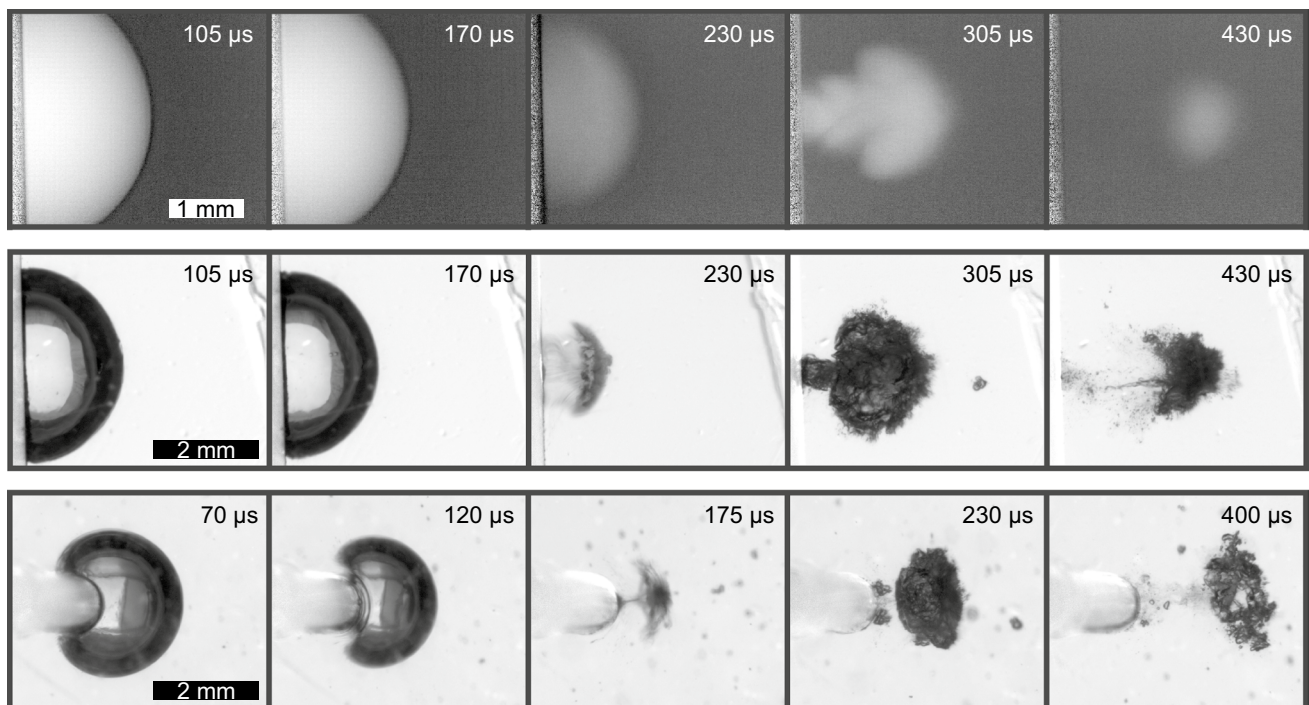

Fig. 1 Selected frames of movies (video in Supporting Information) recorded with X-ray (top) and optical imaging (middle, bottom) of ablation on a Zn wire (1 mm) with a pulse energy of 11 mJ. Top and middle frames are taken perpendicularly to the wire, the bottom row with viewing direction parallel to the wire, all with the wire on the left side and the laser coming from the right side. From left to right: maximum expansion of first bubble; beginning of a rim near target (in particular in bottom row); collapse of the first bubble; first rebound and second rebound, respectively. Note the smaller volume of the bubble along the wire due to measurements in a different chamber with a higher colloidal concentration

of the target (to the left) as the target does hardly transmit X-rays and does not transmit visible light, respectively.

X-ray and UV–Vis absorption spectroscopy X-ray absorption spectroscopy was performed at the synchrotron at KIT (Karlsruhe, Germany) on the micro-beam spectroscopy setup SUL-X. A (111) double-crystal monochromator selects the X-ray energy. The X-rays are detected in an ionization chamber for incoming flux and a 7-element fluorescence detector (Si(Li), Gresham) in 90° geometry for the fluorescence yield. As reference substances, a zinc foil was measured in transmission geometry, ZnO and hydrozincite $(Zn_5(CO_3)_2(OH)_6)$ as cellulose pellets and $ZnCl_2$ as solution in fluorescence geometry (Sigma-Aldrich). Quick near-edge (XANES) curves were acquired with a dwell time of 1 s per energy point. Longer scans at the end of oxidation for a full-extended spectrum (EXAFS) of the ageing run were acquired with improved statistics. Data analysis was performed by means of the software package IFFEFIT, in particular ATHENA [27]. The XANES spectra from a 50-min ageing run were analysed by single value decomposition [28, 29] to reveal the main spectral components of the batch. Additionally, slices at the characteristic energies of metallic zinc (9660 eV) and ZnO (9668 eV) were derived and normalized to the relative content of both.

UV–Vis absorption spectroscopy was performed with a deuterium light source (DH-2000, Ocean Optics) and a fiber-coupled spectrometer (USB2000, Ocean Optics). Spectra were measured for 10 ms and averaged over 100 subsequent ones. Note that the used PMMA cuvette has its cut-off at around 255 nm and extinction, therefore, is not reliable below this wavelength.

Powder diffraction Powder diffraction has been performed on an amount of dried nanoparticle suspension on a silicon wafer. The instrument is a copper-sealed anode tube with Bragg-Brentano geometry (X'Pert Pro, Panalytical).

3 Results and discussion

Recent PLAL studies have clarified the typical macroscale bubble dynamics and the related appearance and reactions of the ablated NPs. In particular, it was found that a large part of the ablated mass is contained in the cavitation bubble [16, 25] induced by the laser impact and the resulting heated plasma [30]. The collapse of this bubble retains the material close to the target surface, while material emission into the bulk water only becoming efficient at later stages [24]. This is problematic for two reasons, first, ablated material may get redeposited onto the target, which limits the efficiency of the NP production. Second, particles residing close to their position of generation may be hit by a subsequent laser pulse if no sufficient liquid transport takes place. Convection, as single means of transport in batch geometry, is only effective on a multi-second time scale. Consequently, at high repetition rates, which are relevant for a high throughput [14], part of the laser beam will be absorbed by these particles to deteriorate the ablation process.

The reason for strong bubble collapse is the high symmetry of the cavitation bubble around the laser impact. A flat target acts simply as a mirror for the hydrodynamical forces leading to a symmetric bubble collapse [31]. A reduction of this symmetry leads to a asymmetry of collapse, with, for instance, formation of jets [32] or rims close to the target [24, 33]. This can be beneficial for enhanced material emission, as shown with different target geometries [15, 19, 25, 34, 35].

We, therefore, adapt a clamped-wire setup, where the wire is transported perpendicularly to the laser beam, but symmetrically surrounded by water. Messina et al. [34] and others [19, 36] have probed the efficiency, which peaked between 0.5 and 0.75 mm wire thickness.

3.1 Bubble dynamics and particle generation on free-standing wire

The images presented in Fig. 1 (video in Supporting Information) show that the first cavitation bubble develops symmetrically upon expansion, but already the shrinking shows a more complex bubble dynamics. A rim arises during the shrinking being most prominent parallel to the wire (Fig. 1 bottom 120 µs), comparable to flat targets [25]. This leads to a loss of contact between bubble and wire even before the first collapse, basically because of a faster bubble shrinking at the higher curvature. The bubble completely detaches with only a little stem remaining (reminding of a mushroom). This mushroom is anisotropic with respect to the wire direction, with the stem being spread along the wire. The further development of the rebounds still contains a component of bubble oscillation, but is strongly overlaid by a fast forward movement of the structure. In visible stroboscopy, the rebounds show up as a dark feature. The first rebound shows substantial X-ray transmission change, which characterizes it as a more or less homogeneous cavity (305 µs). This changes with the second rebound (430 µs), which turns completely opaque in the visible image and only slightly changed X-ray transmission. Therefore, we believe that the latter represents a cloud of microbubbles [37] rather than one homogeneous cavity. At this time delay, the plume has already been displaced some 2 mm from the target.

The ablation yield can be enhanced by changing the target geometry [34]. As shown in Fig. 1, using a wire target leads to a detachment of the bubble collapse from the sample. Therefore, the redeposition of the NPs can be hindered. In addition, increasing the pulse frequency in a scanner system can enhance the ablation yield. This allows for spatially bypassing the ablation bubble, which can lead to an ablation

rate of up to 4 g/h [14]. In our case, the limitation in pulse frequency is still present, in particular with perpendicular excitation. However, a more oblique laser beam incidence could in principle again bypass the cavitation bubble.

We experienced one further limitation of high ablation yields. Particles being already present in the water shield the laser, and therefore, reduce the laser energy of subsequent shots reaching the target. The NP appearance can even be seen by eye as a greyish dyeing of the liquid. This would lead to a strongly decreasing bubble size (by 50% within the first 100 shots at a steady water column, data not shown), and therefore, to a decreased ablation rate [30]. Therefore, the number of shots in the batch was limited to ≤1000. Re-irradiation and consequently fragmentation has likely occurred [38], possibly decreasing particle size and also narrowing the size distribution [39].

3.2 Particle oxidation

Zn and especially ZnO are of importance in many fields, therefore, the oxidation process from freshly ablated metallic Zn to oxidized ZnO particles is of major interest. In agreement with earlier studies [5, 6], we record a change in the extinction spectra of freshly ablated particles on a minute time scale. As shown in Fig. 2, the extinction starts with a Drude-like behavior of metallic zinc and develops into a band gap behavior of ZnO within the first 10 min (solid lines). Afterwards, only the global extinction decreases slowly due to slight sedimentation (dashed lines), but the ratio between the extinction at 275 nm and 330 nm does not change any more as shown in the inset of Fig. 2.
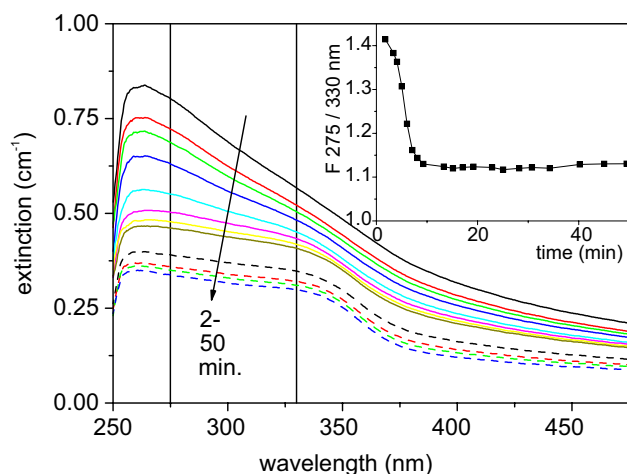
Optical spectroscopy is a versatile and easy method to record changes of samples which manifest in the optical extinction. However, extinction is sensitive on many aspects, such as absorption and scattering of the system as a whole. The extinction changes on the time scale of minutes due to several mechanisms as the here shown chemical changes or ripening and growth processes [40, 41]. In addition, particle–particle interactions or particle–solvent interaction might be overlaid non-specifically. In contrast to that, X-ray absorption spectroscopy is directly sensitive to the electronic and local atomic structure of the selected atomic species without disturbance by the exterior.

Therefore, we performed X-ray absorption measurements on ablated Zn NPs. The X-ray absorption spectrum of a NP suspension after 5 h of ageing is shown in Fig. 3. It is normalized relative to free-atom absorption and flattened for the post-edge region according to the standard approaches in XAS by means of the ATHENA software.

The signature of the EXAFS oscillations is reproduced by the sum of references of ZnO powder and hydrozincite, with some small contribution of zinc metal. Metallic zinc is more easily discerned in the near-edge structure. The metal spectrum is characterized by an absorption onset at lower energy as compared to ZnO and hydrozincite. The entire near-edge region can only be explained by adding the contribution on ZnO (tetrahedrally coordinated) and hydrozincite (tetrahedrally and octahedrally coordinated). A further test on octahedral coordination purely with OH ions, as an indicator for $Zn(OH)_2$ was done by comparison with the dissolved $ZnCl_2$ as reference [42]. This did not lead to better fits of the nanoparticle XAS curve, as in terms of coordination and spectral distribution $ZnCl_2$ and hydrozincite are very similar.

Fig. 2 UV–Vis extinction spectra of ablated Zn NPs at different time delays after ablation. The inset shows the ratio between the extinction at 275 and 330 nm. Spectra change from metallic Zn (peak near 250 nm) to more or less ZnO behavior (plateau under 340 nm [5]) within 10 min
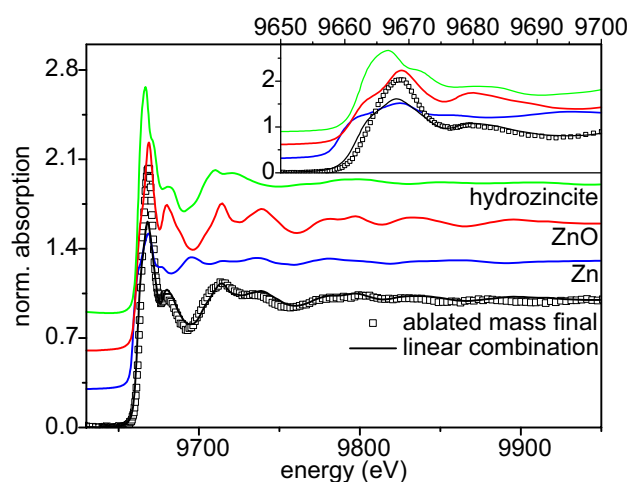

Fig. 3 X-ray absorption spectrum of a Zn oxide nanoparticle suspension after 5 h ageing time. The lines are the reference spectra for a hydrozincite powder, Zn foil and ZnO powder. The reference spectra are shifted by 0.3 each for a better visibility

Reports state that hydrozincite is the more stable product compared to ZnO and $Zn(OH)_2$, the latter only dominating at high pH [43, 44].

A fit with the three references returns $(45 \pm 5)\%$ ZnO, $(45 \pm 5)\%$ hydrozincite and below 10% of metallic zinc. Furthermore, the findings are supported by powder diffraction of NPs obtained from PLAL of Zn in water as depicted in Fig. 4. It not only shows primarily oxidized particles composed of ZnO but also a significant amount of hydrozincite and amounts of metallic Zn. While the Zn peaks are relatively strong, a quantitative estimate of composition is not possible due to the unknown long range order of the species (crystalline quality). The involved carbon is most probably introduced by the carbon dioxide which is dissolved in the water. Note that oxygen is always present due to the laser hydrolysis occurring during the ablation even in degassed water [37, 45].

The largest absolute differences between metallic and oxide Zn in the X-ray absorption spectrum are located in the XANES region. Therefore, time-resolved scans directly after the ablation have been acquired between 9650 and 9710 eV. Selected spectra are shown in Fig. 5. Indeed, one can detect a continuous change with time in this range. The absorption decreases steadily at around 9660 eV and increases at around 9668 eV, which already indicates a transition from metallic material to a contribution of oxides.

A singular-value decomposition was performed on the set of curves by means of the package ATHENA. As a result, three contributions show a considerable share to the data (see Fig. 6). Interestingly, contribution 0, the base curve, is resembling the overall shape of the absorption structure at the Zn-K edge with resemblance to the ZnO spectrum. Contribution 1 is a difference structure that is positive at
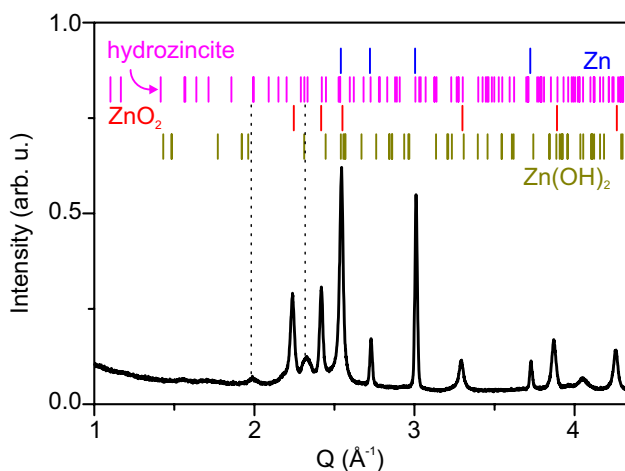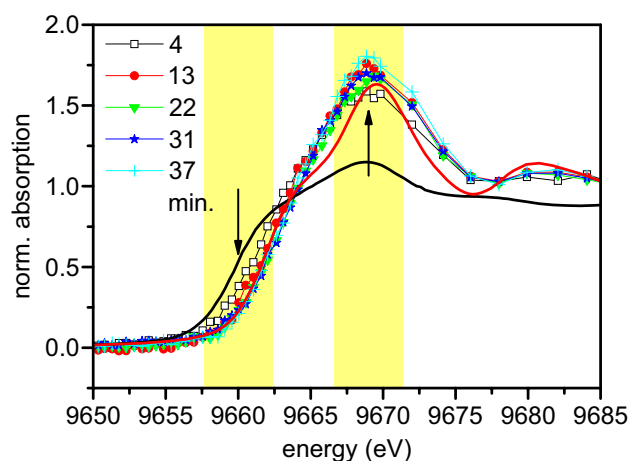

Fig. 5 Change of the near-edge absorption spectrum as function of delay after ablation. The shown curves with symbols are taken at 4, 13, 22, 31 and 37 min. The lines depict the spectra for pure Zn (black) and ZnO (red) for reference. The shaded areas around 9660 and 9668 eV mark the intervals that are used for extraction of Zn and hydrozincite content

around 9660 eV and negative at around 9670 eV. In fact, comparing it to the difference curve between metallic Zn and ZnO shows a very strong agreement. Finally, contribution 2 is a non-specific spectral dip around the edge, which we do not directly identify with an intermediate state. It may reflect a contribution from hydrozincite with an absorption peak shifted to lower energies as compared to ZnO. It can rather reflect an amount of structural disorder by damping spectral features. Indeed, in a repetition of the experiment, this feature is not well reproducible. This leads us to the conclusion that two major components are involved in the chemical
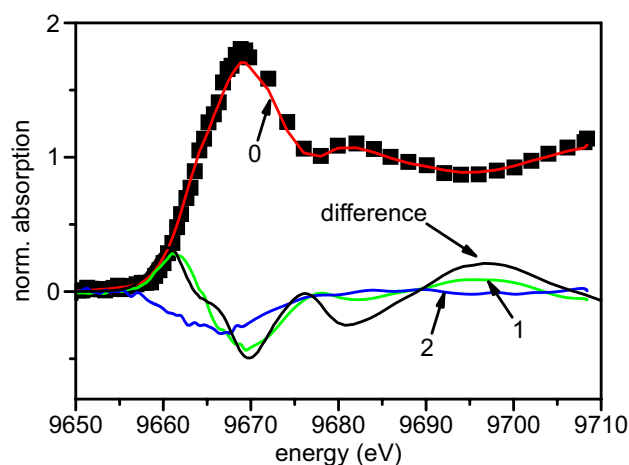

Fig. 4 Powder diffractogram of a dried suspension of ablated nanoparticles together with the location of presumed crystalline components

Fig. 6 Near-edge absorption spectrum after 50-min ageing (filled squares) together with the first 3 singular values from singular-value decomposition. The black line is generated from a difference of the Zn foil to ZnO powder

reaction during ageing of the suspension. This ageing can be directly explained by an ongoing oxidation. This is in line with earlier observations [5, 6], where an oxidation of ablated or chemically produced Zn/ZnO NPs is reported to proceed on a time scale of several minutes which is in good agreement with our findings. The contribution of hydrozincite to the spectra after a few minutes is minor.

To quantify the oxidation process, we have derived absorption values as function of delay at the selected energies of 9660 and 9668 eV and normalized these values relative to the isosbestic point at 9690 eV for a relative content of metallic and oxidized zinc. The temporal change of this share is plotted in Fig. 7. Additionally, we included the change in ratio of the UV–Vis extinction spectroscopy as shown in the inset of Fig. 2. Therefore, we assume a simple oxidation from metallic to Zn(II), which occurs within the time scale of a few minutes. Earlier reports assume a transition via a core-shell-like structure with the metal being surrounded by a growing oxidic shell [5]. While the UV–Vis extinction indicates the end of oxidation within 10 min, the XANES data still show some drift in contribution up to 30 min, while the main changes are in the first minutes. A significantly increasing hydrozincite contribution could not be verified. Therefore, we assume the fast reaction of the freshly ablated zinc consists in oxidation to form ZnO. Indeed, oxygen may readily be available in the liquid due to the generation of permanent gas at the ablation [36]. Only later a quantitative transformation into hydrozincite takes place. The necessary carbon is available through air, as no sealed container were used. The extended X-ray absorption spectra reveal that both ZnO and hydrozincite show a long range order beyond the first coordination shell. This indicates their presence in a solid form.
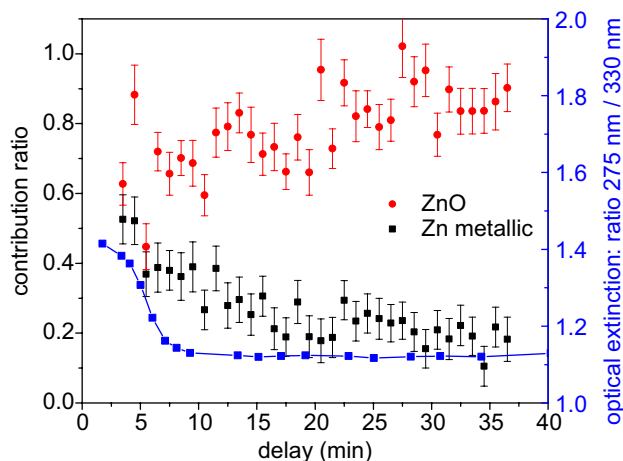
4 Conclusion

We have investigated the production of Zn/ZnO NPs by pulsed laser ablation of a Zn wire in water with nanosecond laser pulses. The use of a customized setup with miniature chamber and transport of liquid and target together with a wire target represents an approach for efficient ablation. The wire target leads to a symmetry breaking of the excited vapor bubble, which has been visualized by both visible-light stroboscopy and X-ray radiography. Both reveal the mushroom-like development of the bubble and its rebounds to quickly transport material away from the target. Additionally, we have no indications for any depression of the bubble on the opposite side to the target or an inward jet during shrinking of the first bubble on wires under a high water column.

Element-specific analysis of the ablated material is performed by time-resolved X-ray absorption spectroscopy, which allows to discern the involved chemical species and the kinetics of the oxidation. Within a minute after ablation, partly oxidized material is detected, the main oxidation takes place within 10 min, while a full oxidation mainly to ZnO takes some 30 min. On longer time scales, a partial transformation into hydrozincite takes place, possibly ruled by CO_2 availability. This latter aspect may be important for understanding the release pathways of zinc ions in applications [46]. X-ray absorption spectroscopy hold prospects to investigate this oxidation or more complicated reactions during PLAL even on a shorter time scale, ideally with microsecond resolution to study the chemical speciation of the particles already within the cavitation bubble [47].

Fig. 7 Temporal change of the contributions from metallic Zn and ZnO as function of aging time after 1 min of ablation

References

1. Ü. Özgür, Y.I. Alivov, C. Liu, A. Teke, M.A. Reshchikov, S. Doğan, V. Avrutin, S.J. Cho, H. Morkoç, J. Appl. Phys. **98**, 041301 (2005)
2. H. Usui, Y. Shimizu, T. Sasaki, N. Koshizaki, J. Phys. Chem. B **109**, 120 (2005)
3. J.M. Cho, J.K. Song, S.M. Park, Bull. Korean Chem. Soc. **30**, 1616 (2009)
4. P. Wagener, A. Schwenke, B.N. Chichkov, S. Barcikowski, J. Phys. Chem. C **114**, 7618 (2010)
5. P. Camarda, L. Vaccaro, F. Messina, M. Cannas, Appl. Phys. Lett. **107**, 013103 (2015)
6. P. Camarda, F. Messina, L. Vaccaro, G. Buscarino, S. Agnello, F.M. Gelardi, M. Cannas, J. Appl. Phys. **120**, 124312 (2016)
7. A. Fojtik, A. Henglein, Ber. Bunsenges. Phys. Chem. **97**, 1493 (1993)

8. F. Mafuné, J. Kohno, Y. Takeda, T. Kondow, J. Phys. Chem B **105**, 5114 (2001)
9. G. Compagnini, A.A. Scalisi, O. Puglisi, Phys. Chem. Chem. Phys. **4**, 27872791 (2002)
10. S. Barcikowski, A. Menéndez-Manjón, B. Chichkov, M. Brikas, G. Račiukaitis, Appl. Phys. Lett. **91**, 083113 (2007)
11. H. Zeng, X.W. Du, S.C. Singh, S.A. Kulinich, S. Yang, J. He, W. Cai, Adv. Funct. Mat. **22**, 1333 (2012)
12. H. Zeng, W. Cai, Y. Li, J. Hu, P. Liu, J. Phys. Chem. B **109**, 18260 (2005)
13. M. Fischer, J. Hormes, G. Marzun, P. Wagener, U. Hagemann, S. Barcikowski, Langmuir **32**, 8793 (2016)
14. R. Streubel, S. Barcikowski, B. Gökce, Opt. Lett. **41**, 1486 (2016)
15. S. Kohsakowski, B. Gökce, R. Tanabe, P. Wagener, A. Plech, Y. Ito, S. Barcikowski, Phys. Chem. Chem. Phys. **18**, 16585 (2016)
16. S. Ibrahimkutty, P. Wagener, A. Menzel, A. Plech, S. Barcikowski, Appl. Phys. Lett. **101**, 103104 (2012)
17. P. Wagener, S. Ibrahimkutty, A. Menzel, A. Plech, S. Barcikowski, Phys. Chem. Chem. Phys. **15**, 3068 (2013)
18. K. Sasaki, T. Nakano, W. Soliman, N. Takada, Appl. Phys. Express **2**, 046501 (2009)
19. A. De Giacomo, M. DellAglio, A. Santagata, R. Gaudiuso, O. De Pascale, P. Wagener, G.C. Messina, G. Compagnini, S. Barcikowski, Phys. Chem. Chem. Phys. **15**, 3083–3092 (2013)
20. T. Sakka, S. Iwanaga, Y.H. Ogata, A. Matsunawa, T. Takemoto, J. Chem. Phys. **112**, 8645 (2000)
21. A. Tamura, A. Matsumoto, K. Fukami, N. Nishi, T. Sakka, J. Appl. Phys. **117**, 173304 (2015)
22. M.R. Gavrilović, M. Cvejić, V. Lazić, S. Jovićević, Phys. Chem. Chem. Phys. **18**, 14629 (2016)
23. L. Lavisse, J.L. Le Garrec, L. Hallo, J.M. Jouvard, S. Charles, J. Perez, J.B.A. Mitchell, J. Decloux, M. Girault, V. Potin, H. Andrzejewski, M.C.M. de Lucas, S. Bourgeois, Appl. Phys. Lett. **100**, 164103 (2012)
24. S. Ibrahimkutty, P. Wagener, T. dos Santos Rolo, D. Karpov, A. Menzel, T. Baumbach, S. Barcikowski, A. Plech, Sci. Rep. **5**, 16313 (2015)
25. S. Reich, P. Schönfeld, P. Wagener, A. Letzel, S. Ibrahimkutty, B. Gökce, S. Barcikowski, A. Menzel, T. dos Santos Rolo, A. Plech, J. Coll. Interf. Sci. **489**, 106 (2017)
26. T. dos Santos Rolo, A. Ershov, T. van de Kamp, T. Baumbach, Proc. Natl. Acad. Sci USA **111**, 3921–3926 (2014)
27. B. Ravel, M. Newville, J. Synchrotron Rad. **12**, 537 (2005)
28. M. Schmidt, R. Pahl, V. Srajer, S. Anderson, Z. Ren, H. Ihee, S. Rajagopal, K. Moffat, Proc. Natl. Acad. Sci. **101**, 4799 (2004)
29. M.F. Lengke, B. Ravel, M.E. Fleet, G. Wanger, R.A. Gordon, G. Southam, Environ. Sci. Technol. **40**, 6304 (2006)
30. S. Reich, P. Schönfeld, A. Letzel, S. Kohsakowski, M. Olbinado, B. Gökce, S. Barcikowski, A. Plech, Chem. Phys. Chem. **18**, 1084 (2017)
31. A. Matsumoto, A. Tamura, A. Kawasaki, T. Honda, P. Gregorčič, N. Nishi, K. ichi Amano, K. Fukami, T. Sakka, Appl. Phys. A **122**, 234 (2016)
32. E.A. Brujan, G.S. Keen, A. Vogel, J.R. Blake, Phys. Fluids **14**, 85 (2002)
33. A. Shima, Y. Sato, Ingenieur. Archiv. **48**, 85–95 (1979)
34. G.C. Messina, P. Wagener, R. Streubel, A.D. Giacomo, A. Santagata, G. Compagnini, S. Barcikowski, Phys. Chem. Chem. Phys. **15**, 3093–3098 (2013)
35. S. Scaramuzza, M. Zerbetto, V. Amendola, J. Phys. Chem. C **120**, 9453 (2016)
36. S. Kohsakowski, A. Santagata, M. DellAglio, A. de Giacomo, S. Barcikowski, P. Wagener, B. Gökce, Appl. Surf. Sci. **403**, 487 (2017)
37. M.R. Kalus, N. Bärsch, R. Streubel, E. Gökce, S. Barcikowski, B. Gökce, Phys. Chem. Chem. Phys. **19**, 7112 (2017)
38. S. Sasaki, H. Ikenoue, T. Tsuji, Y. Ishikawa, N. Koshisaki, Chem. Phys. Chem. **18**, 1101 (2017)
39. M. Procházka, P. Mojzeš, J. Štěpánek, B. Vlcková, P.Y. Turpin, Anal. Chem. **69**, 5103 (1997)
40. B. Gökce, D.D. van 't Zand, A. Menendez-Manjon, S. Barcikowski, Chem. Phys. Lett. **626**, 96 (2015)
41. S. Jendrzej, B. Gökce, V. Amendola, S. Barcikowski, J. Coll. Interf. Sci. **463**, 299 (2016)
42. P. D'Angelo, A. Zitolo, F. Ceccacci, R. Caminiti, G. Aquilanti, J. Chem. Phys. **135**, 154509 (2011)
43. A. Moezzi, M. Cortie, A. McDonagh, Dalton Trans. **40**, 4871 (2011)
44. P. Kowalik, M. Konkol, K. Antoniak-Jurak, W. Próchniak, P. Wierciocha, M. Rawski, T. Borowiecki, Mat. Res. Bull. **65**, 149 (2015)
45. C.L.B.C.W.B.B.G. Marzun, H. Bönnemann, Chem. Phys. Chem. **18**, 1175 (2017)
46. R.B. Reed, D. Ladner, C.P. Higgins, P. Westerhoff, J. Ranville, Environ. Toxicol. Chem. **31**, 93 (2012)
47. A. Letzel, B. Gökce, P. Wagener, S. Ibrahimkutty, A. Menzel, A. Plech, S. Barcikowski, J. Phys. Chem. C **121**, 5356 (2017)